



Ultra-low-threshold continuous-wave and pulsed lasing in tensile-strained GeSn alloys

Anas Elbaz^{1,2}, Dan Buca³✉, Nils von den Driesch^{3,4}, Konstantinos Pantzas¹, Gilles Patriarche¹, Nicolas Zerounian¹, Etienne Herth¹, Xavier Checoury¹, Sébastien Sauvage¹, Isabelle Sagnes¹, Antonino Foti⁵, Razvigor Ossikovski⁵, Jean-Michel Hartmann⁶, Frédéric Boeuf², Zoran Ikonc⁷, Philippe Boucaud⁸, Detlev Grützmacher^{3,4} and Moustafa El Kurdi¹✉

Strained GeSn alloys are promising for realizing light emitters based entirely on group IV elements. Here, we report GeSn microdisk lasers encapsulated with a SiN_x stressor layer to produce tensile strain. A 300 nm-thick GeSn layer with 5.4 at% Sn, which is an indirect-bandgap semiconductor as-grown, is transformed via tensile strain engineering into a direct-bandgap semiconductor that supports lasing. In this approach, the low Sn concentration enables improved defect engineering and the tensile strain delivers a low density of states at the valence band edge, which is the light hole band. We observe ultra-low-threshold continuous-wave and pulsed lasing at temperatures up to 70 K and 100 K, respectively. Lasers operating at a wavelength of 2.5 μm have thresholds of 0.8 kW cm⁻² for nanosecond pulsed optical excitation and 1.1 kW cm⁻² under continuous-wave optical excitation. The results offer a path towards monolithically integrated group IV laser sources on a Si photonics platform.

Si-Ge-Sn alloys are a promising, enabling material system for the monolithic integration of both passive and active optoelectronic devices and circuits on Si (ref. ¹). At present, Si photonics relies on the integration of III-V materials for emitters². Although such an approach has recently demonstrated some impressive progress, it still faces challenges such as wafer throughput, scalability and compatibility with the current Si complementary metal-oxide-semiconductor (CMOS) technology. The most successful route to laser action within group IV materials is currently based on GeSn semiconductors. The first demonstration of an optically pumped laser³ and subsequent developments to improve the performance in terms of threshold and operation temperature⁴⁻⁷ have shown the potential of these group IV materials for achieving Si-based light sources, the final ingredient for completing an all-inclusive nanophotonic CMOS platform. Furthermore, (Si)GeSn materials can help to extend the present Si photonics platform to a much broader application area than only near-infrared data communication. In the short-wave to mid-infrared region of 2–4 μm, in which GeSn laser emission has been obtained, potential applications can be envisaged such as gas sensing for environmental monitoring and industrial process control⁸, lab-on-a-chip applications^{9,10} or infrared imaging for night vision and hyperspectral imaging¹¹.

An increase in the Sn content of GeSn alloys modifies the energy of the electronic bands. The bandgap at the Γ point (E_{Γ}) reduces more quickly than the bandgap towards the L valley (E_L), leading to a crossover from an indirect- to a direct-bandgap semiconductor at a Sn concentration of 8 at% (ref. ³). The lattice mismatch between Sn-containing alloys and the Ge buffer layer, the typical virtual substrate for their epitaxial growth, generates compressive strain in the grown layer, which counteracts the effect of Sn incorporation, decreasing the directness $\Delta E_{L-\Gamma} = E_L - E_{\Gamma}$. In contrast, the application

of tensile strain will increase the directness. Finding a proper balance between having a moderate Sn content to minimize crystal defects and maintain the thermal stability of the GeSn alloy on the one hand and making use of tensile strain on the other hand are the keys to bringing the lasing threshold and operation temperature close to an application's requirements. Mainstream research to increase $\Delta E_{L-\Gamma}$ focuses on high-Sn-content alloys^{5,12}, obtained by epitaxy of thick strain-relaxed GeSn layers. A large directness is obtained, leading to higher-temperature operation, but at the expense of a steadily increasing laser threshold¹³. We have recently proposed an alternative theoretical approach that is based on two key features: employing moderate-Sn-content GeSn alloys and inducing tensile strain in them¹⁴. Our study indicated that, if a given directness is reached via tensile strain rather than by increasing the Sn content, the material can provide a higher net gain. The underlying physics originates in valence band splitting and lifting up of the light hole (LH) band above the heavy hole (HH) band. Its lower density of states (DOS) reduces the carrier density required for transparency, hence reducing the lasing threshold, as will be shown in the following.

GeSn alloys with a moderate Sn content offer a couple of advantages from a materials perspective. The epitaxial growth temperature, 375 °C (compared to below 300 °C for high-Sn-content alloys), yields a better crystalline quality and lower defect density. Lattice mismatch and, therefore, the density of misfit dislocations at the GeSn/Ge interface scale with Sn content¹⁵. Both types of defect strongly influence the carrier recombination dynamics^{16,17} and contribute to the high pumping levels necessary to reach lasing. Accordingly, laser thresholds of 100–300 kW cm⁻² have been reported at 20 K for GeSn lasers with 12–14 at% Sn (refs. ^{4,18}), while values on the scale of ~MW cm⁻² are required for very-high-Sn-content alloys (>20 at%) above 230 K (refs. ^{7,12}).

¹Center for Nanoscience and Nanotechnology, C2N UMR 9001, CNRS, Université Paris Sud, Université Paris Saclay, Palaiseau, France. ²STMicroelectronics, Crolles, France. ³Peter Grünberg Institute (PGI 9) and JARA-Fundamentals of Future Information Technologies, Forschungszentrum Juelich, Juelich, Germany. ⁴JARA-Institute Green IT, RWTH Aachen, Aachen, Germany. ⁵LPICM, CNRS, Ecole Polytechnique, Université Paris-Saclay, Palaiseau, France. ⁶CEA, LETI and Univ. Grenoble Alpes, Grenoble, France. ⁷Pollard Institute, School of Electronic and Electrical Engineering, University of Leeds, Leeds, UK. ⁸Université Côte d'Azur, CNRS, CRHEA, Valbonne, France. ✉e-mail: d.m.buca@fz-juelich.de; moustafa.el-kurdi@u-psud.fr

The described material advantages and the underlying physics should then be combined with the technology able to induce tensile strain in GeSn alloys. Strain engineering is a mature Si technology employed to modify the electronic band structure of semiconductors¹⁹. In pure Ge, 1.7% biaxial^{20,21} or 4.5% uniaxial^{22–24} strain is required to energetically align the L and Γ valleys ($\Delta E_{L-\Gamma} = 0$), that is, to reach crossover from an indirect to a direct semiconductor. Even higher strain is required to achieve the mandatory directness, $\Delta E_{L-\Gamma} > 150$ meV, for room-temperature operation of a strained Ge laser. Although such high levels of tensile strain are technologically possible^{25,26}, they are challenging in a laser device geometry. Depending on the Sn content, which can be chosen in the range of 5–8 at%, significantly lower values of tensile strain are needed in GeSn alloys to achieve a sufficient directness¹⁴. However, to obtain a laser with low pumping threshold, the impact of the defective GeSn/Ge interface region has to be removed. This is responsible for a considerable part of non-radiative recombination. The growth of hetero and quantum well (QW) structures appears to be a suitable technology to separate the gain material from the defective interface¹⁷. Here, we focus on the impact of tensile strain and, for simplicity, we are using bulk GeSn layers. To remove the defective interface, the layer transfer method is applied, as used to fabricate GeSn on insulator (GeSnOI) structures. Due to the transfer, the defective part is at the top surface of the GeSn layer and can be removed easily by etching.

All GeSn lasers reported in the literature so far operate only under pulsed excitation, although continuous-wave (c.w.) lasing is the key milestone required for accessing the full potential of GeSn for technologically useful optical devices. In this work, we demonstrate both c.w. and pulsed lasing using microdisk cavities fabricated from initially indirect-bandgap $\text{Ge}_{0.946}\text{Sn}_{0.054}$ alloys. A tensile strain of 1.4% is applied *ex situ* to the GeSn layer, using all-around SiN_x stressors. The method relies on the formation of GeSnOI by wafer bonding and layer transfer, followed by under-etching so that the final cavity is supported by a metallic post, here Al, that acts as a heat sink. The combination of these factors—that is, strain engineering, bulk defect density reduction and improved heat removal—allows the demonstration of lasing in tensile-strained GeSn with low thresholds of 0.8 kW cm^{-2} and 1.1 kW cm^{-2} at 25 K in pulsed and c.w. operation regimes, respectively. The threshold is two orders of magnitude lower than previously reported for GeSn pulsed lasers, while no reports of c.w. lasing in GeSn are available.

Results

Material growth, characterization and cavity patterning. The GeSn layers were grown on Ge virtual substrates (Ge-VS) on 200 mm Si(100) wafers^{4,18} via reactive gas source epitaxy using an AIXTRON TRICENT reactor²⁷. Digermane (Ge_2H_6) and tin tetrachloride (SnCl_4) were used as precursors for elementary Ge and Sn, respectively. GeSn layers with thicknesses of 300 nm and Sn content of 5.4 at% were grown at 375 °C. The layers were partially strain-relaxed, with a residual compressive strain of -0.32% as measured by X-ray diffraction (Fig. 1a). Details on the material characterization are provided in the Supplementary Information.

The GeSn layers were processed into microdisk cavities with all-around SiN_x stressors. The technology flow, developed for pure Ge²⁸ and adapted for GeSn thermal budget limitations²⁹, is presented in the Supplementary Information. Some key aspects are shown in Fig. 1b. The stressor layer is a 350 nm-thick SiN_x layer with an intrinsic stress of -1.9 GPa. An additional Al metal layer was added to the layer stack to reduce heating during optical pumping^{30,31}. This is particularly important, because alloying of Ge with Sn strongly decreases the thermal conductivity of the alloy³². After GeSn bonding and removal of the donor wafer, the top 40 nm of the GeSn layer, containing the defective GeSn/Ge interface, was also removed. It was shown that this dense misfit network strongly reduces the

photoluminescence (PL) of the layers at the onset of strain relaxation³³. Up to this step, the compressive strain in the GeSn layer is preserved (Fig. 1c,d). Tensile strain, coming from the SiN_x stressor underneath, is induced only by structuring the GeSn/ SiN_x layer stack (Fig. 1b). The under-etching process—that is, selective and local removal of Al—was optimized to maximize the tensile strain in the GeSn layer and achieve a wide Al post for heat sinking. Subsequently, the suspended disks were conformally covered by a second 400 nm-thick SiN_x stressor layer, leading to fully encapsulated GeSn disks, standing on Al posts (Fig. 1b). This layer transfer technology and processing transforms the initial $\text{Ge}_{0.946}\text{Sn}_{0.054}$ layer with residual compressive strain and an indirect bandgap into a microdisk exhibiting pronounced biaxial tensile strain and consequently a direct bandgap.

Sample analysis. Raman spectroscopy was performed to follow the strain evolution during fabrication of the GeSn microdisks. The positions of the Ge-Ge vibration modes in GeSn alloys in the as-grown sample are shown in Fig. 1c (blue line), after bonding onto the host Si substrate (green line) and in the final processed microdisk structure. The Raman modes of the unpatterned transferred layer and the as-grown layer, at 297.3 cm^{-1} and 296.8 cm^{-1} , respectively, are very similar, within the experimental resolution of 0.5 cm^{-1} . Therefore, it can reasonably be assumed that the layer transfer process itself does not change the strain in the GeSn layer. However, after processing of the final microdisk, a Raman shift of -10.5 cm^{-1} is detected. Using the equations from ref. ³⁴, including alloy disorder and strain effects, this Raman shift corresponds to a built-in biaxial tensile strain of 1.5% for the all-around embedded GeSn disk. Note that Raman spectroscopy probes only the in-plane strain within a small depth below the disk surface, while PL probes the whole disk volume, giving an average value of the strain, and is directly related to the band structure²⁸.

The PL experiments were conducted to assess the strain-induced band structure changes, as well as the quality improvement of the transferred layer. The PL signal from the as-grown GeSn layer is very weak due to (1) the indirect bandgap, with the conduction band energy splitting $\Delta E_{L-\Gamma} = -60$ meV, and (2) the presence of defects at the GeSn/Ge interface. After the layer is transferred, these defects are removed and an increase in PL intensity is observed (Fig. 1d). The PL signal is found in the same energy range, indicating again that the transferred layer maintains its compressive strain and, therefore, its indirect bandgap character with L and HH as conduction and valence band extrema, respectively. The optical transition at 0.61 eV is attributed to the recombination of electrons in the L valley of the conduction band and holes near the Γ point of the HH valence band, thus across the fundamental indirect bandgap. Indirect carrier recombination dominates over the direct transitions, because almost 100% of electrons at 20 K are in the L valley. The shoulder of the PL signal around 0.66 eV is assigned to the direct transition, that is, electrons and heavy holes around the Γ point in *k*-space. Details on optical transition identification are provided in the Supplementary Information. The PL spectra in Fig. 1d for the as-grown and transferred GeSn layers were taken under identical conditions with a sensitive InGaAs detector. This is emphasized, because this initially weakly emitting layer will become the active laser medium after inducing tensile strain.

The major limitation for the GeSn emission efficiency, the indirect bandgap, is overcome by tensile strain turning it into a direct-gap semiconductor. Because the extended InGaAs detector has a cutoff wavelength of $2.4 \mu\text{m}$, another set-up with a nitrogen-cooled InSb detector with a cutoff of $4.8 \mu\text{m}$ was used for the fully processed microdisk device. Even though the InSb detector has a lower sensitivity, a strong increase of the integrated PL emission by two orders of magnitude compared to the as-grown layer is measured. The PL signal is strongly redshifted, showing peak emission around

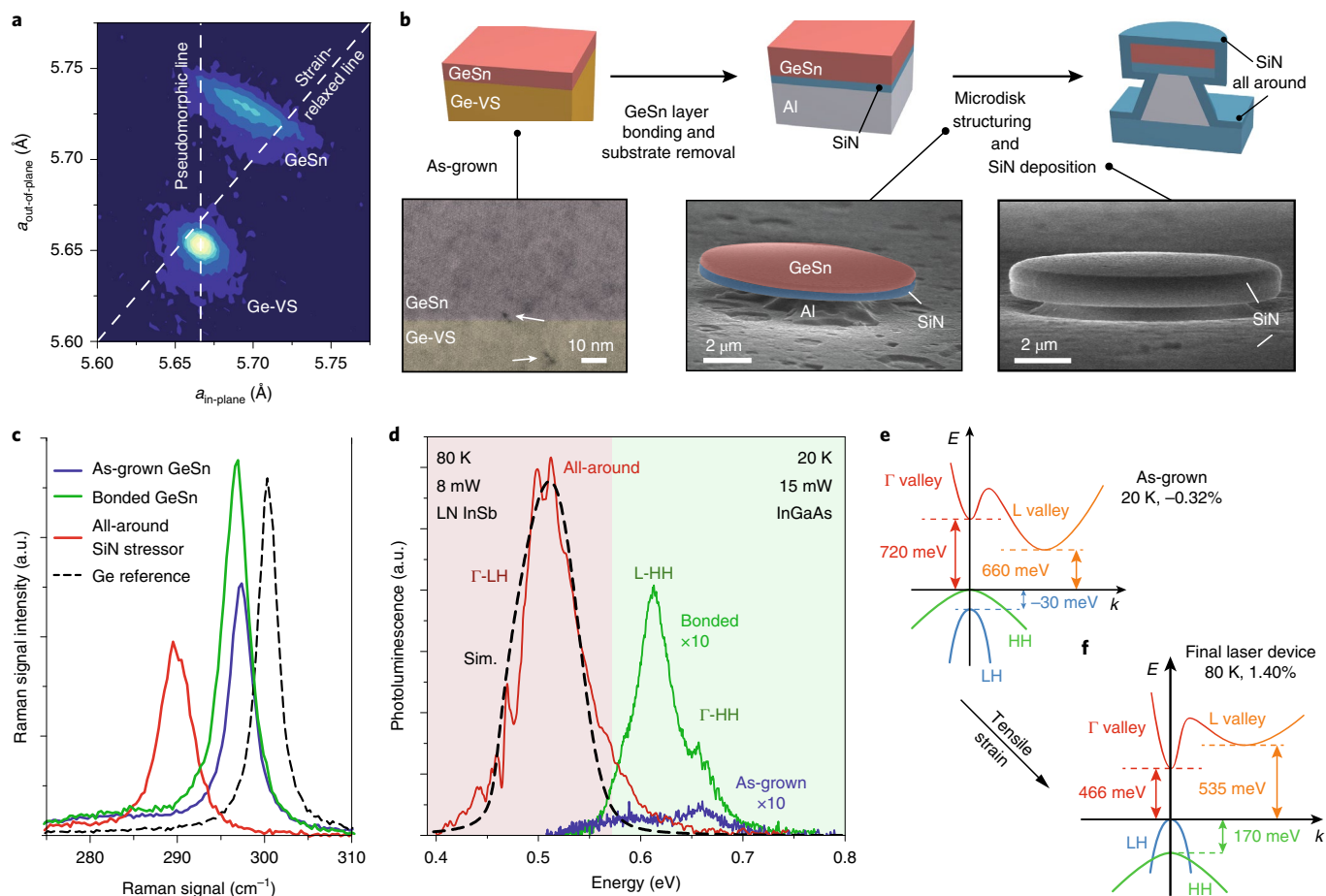


Fig. 1 | Structural and optical characterization. **a**, X-ray diffraction reciprocal space map for quantitative assessment of the layer strain (-0.32%), a is the in-plane and the out-of-plane lattice parameter. **b**, Top: sketch of the processing steps. Bottom left: transmission electron microscopy (TEM) image of the as-grown layer with strain releasing dislocations at the GeSn/Ge-VS interface. Bottom middle and right: scanning electron microscopy (SEM) images of the under-etched GeSn/SiN_x stack and the final laser structure with SiN_x all around. **c**, Raman spectra for three cases: an as-grown layer, a bonded (transferred) layer and an all-around disk with diameter of $9\ \mu\text{m}$. Bulk Ge is used as a reference. **d**, Photoluminescence (PL) spectra taken at 20 K for the as-grown and bonded GeSn layers (the bonded layer has the misfit dislocation network removed) and PL spectrum of the patterned disk with all-around stressor, at 80 K. The dashed line shows the simulated PL spectrum of the final structure. **e, f**, Calculated band structures for the indirect-bandgap as-grown layer (**e**) and direct-bandgap tensile-strained GeSn layer (**f**).

$0.50\ \text{eV}$ which is attributed to the tensile strain of the final structure with the all-around SiN_x stressor. The band structure was modelled using the $\mathbf{k}\cdot\mathbf{p}$ method, with 5.4% Sn and a bandgap of $465\ \text{meV}$ of the strained film. The best fit to the experimental data in Fig. 1d is obtained for a biaxial tensile strain of 1.4% . This value is slightly smaller than the 1.5% obtained from Raman spectroscopy. The discrepancy is attributed to the uncertainty of the parameters used in the two methods. The band structures of the as-grown and tensile-strained GeSn are shown in Fig. 1e,f, respectively. In the final device, the tensile strain lifts the degeneracy of the LH and HH bands, with LH becoming the fundamental valence band. The valence band splitting is $E_{\text{LH}} - E_{\text{HH}} = 170\ \text{meV}$. More importantly, in the conduction band the tensile strain shifts the Γ valley below the L valley. The tensile-strained GeSn thus becomes a direct-bandgap material with a directness of $\Delta E_{\text{L}-\Gamma} = 70\ \text{meV}$. Consequently, the pronounced enhancement of the PL intensity emission is due to the fundamental direct optical transition. The electrons recombine with LH at the Γ point in the centre of the Brillouin zone. This transition is labelled the Γ -LH optical transition.

Continuous-wave device results. To obtain stimulated emission, microdisk devices with a diameter of $9\ \mu\text{m}$ were optically pumped

using a micro-PL ($\mu\text{-PL}$) set-up with $1,550\ \text{nm}$ wavelength c.w. pump laser focused on the sample surface into a $12\ \mu\text{m}$ -diameter spot (see Methods). PL emission spectra collected at various incident pump powers at $25\ \text{K}$ are shown in Fig. 2a. At low excitation levels, the microdisks produce a broad spontaneous emission background, attributed to $\Gamma \rightarrow \text{LH}$ direct transitions. By increasing the c.w. pump power from $0.2\ \text{mW}$ to $0.8\ \text{mW}$, whispering gallery modes (WGMs) develop and grow in intensity on top of the spontaneous emission. Higher excitation induces an exponential intensity increase of the main optical mode at $485\ \text{meV}$. At $2.3\ \text{mW}$ pump power, the lasing emission is four orders of magnitude stronger than the background, as shown in the high-resolution spectrum in Fig. 2b. The two symmetric side lobes of the modes are only a measurement artefact stemming from the finite range of sampling points due to the apodization of the interferogram³⁵.

The observation of a clear threshold in the light-in light-out (L-L) characteristic visible in Fig. 2c,d, the S-shaped L-L characteristic (inset, Fig. 2d) and the collapse of the linewidth (Fig. 2c) unambiguously prove the onset of lasing. The emission energy at $25\ \text{K}$ of the lasing mode at $485\ \text{meV}$ corresponds to $2.55\ \mu\text{m}$ wavelength. WGM simulations (see Methods) indicate that this mode is the transverse magnetic $\text{TM}_{20,1}$ mode. The intensity of this mode

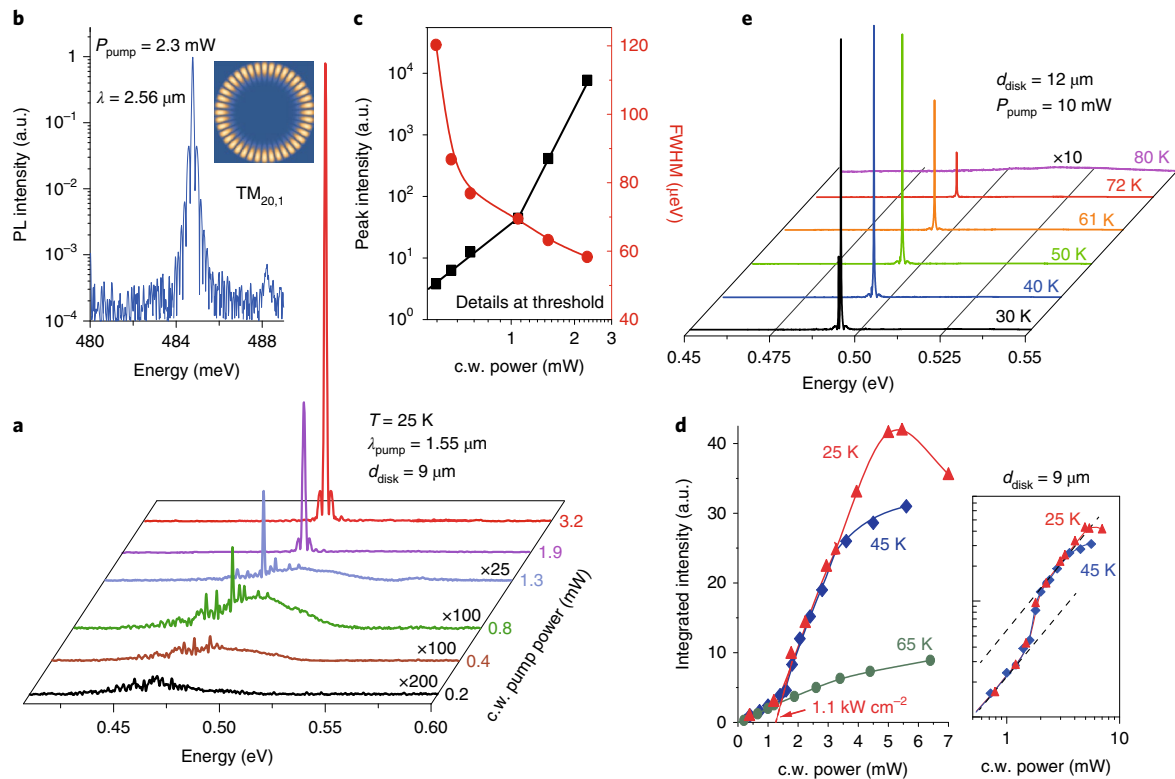


Fig. 2 | Continuous-wave lasing from GeSn. **a**, Emission spectra measured at 25 K for the 9 μm -diameter disk under various c.w. excitation levels. **b**, Lasing mode peak intensity above threshold in logarithmic scale, highlighting its high intensity compared to the spontaneous background emission. The intensity profile of the lasing mode, identified as $\text{TM}_{20,1}$, is shown in the inset. **c**, Detailed behaviour at threshold: L-L curve of the peak intensity of the 485 meV laser mode (black) and its linewidth (red). **d**, L-L curves of the integrated spectra at different temperatures (on logarithmic scales in the inset). The lasing threshold is extracted as 1.3 mW (see Supplementary Information), corresponding to 1.1 kW cm^{-2} . **e**, PL spectra measured on a 12 μm -diameter disk under c.w. pump power of 10 mW at various temperatures from 30 to 80 K, showing lasing operation up to 72 K.

in the threshold region is displayed in Fig. 2c as a function of incident pump power by the L-L characteristics on logarithmic scales. The observed narrowing is consistent with the Schawlow–Townes equations, which predict a decrease by a factor of two at the transition from incoherent to coherent emission. Note that the measured linewidth of 58 μeV is the smallest reported so far for any group IV semiconductor lasers.

The laser threshold, clearly separating the spontaneous and amplified emission regimes, is extracted as 1.3 mW (Fig. 2d). This value corresponds to a pump power density of 1.1 kW cm^{-2} . The dependence of the integrated signal on c.w. pumping power at different temperatures is also shown in Fig. 2d. The typical laser S-shaped emission is shown in logarithmic scales in the inset. Below 45 K, an unambiguous threshold can be observed, while no signature of lasing is detected above 45 K. A rollover of the integrated emission occurs for pump powers above 5 mW. In III–V compounds this effect is typically associated with thermal effects, leading to a sharp laser emission quenching with further increase of temperature. However, for the GeSn microdisk laser under investigation, the directness $\Delta E_{\Gamma-\Gamma}$ is in the range of only 70 meV. In fact, band-filling effects of the Γ valley will reduce the electrons' energy required for thermal (scattering) escape from Γ into the L valley even further. Therefore, a small increase in temperature or excitation power may lead to an exponential increase of this thermal escape, producing the observed rollover. As will be discussed later, an increase in the electron population of the L valley leads to a decrease of the total gain. Microdisks with a diameter of 12 μm were also fabricated. The under-etching is kept constant, leading to the same biaxial tensile strain in the GeSn suspended area where the WGMs are

formed. The laser emission at 489 meV is only 4 meV higher than in 9 μm -diameter disks. One major difference here is that the Al support pillar is much larger now, enabling better heat dissipation. The 12 μm -diameter disk can support the c.w. lasing up to 72 K. The PL spectra are plotted versus temperature in Fig. 2e. The same laser threshold is obtained as for the smaller 9 μm -diameter disks and increases with temperature, reaching $\sim 5 \text{ mW}$ at 72 K (for details see Supplementary Information). An estimation of the disk heating under optical pumping, using finite-element modelling (FEM)^{30,36}, is provided in the Supplementary Information.

The PL spectra of a 9 μm -diameter disk taken at excitation powers below the lasing threshold are shown in Fig. 3a. Assuming a constant temperature of 25 K, spontaneous emission spectra were calculated for different carrier densities to reproduce the broadening of the emission and its blueshift when the pump power increases. The emission blueshift, observed experimentally when increasing the pump power, can be attributed to the band-filling effect inducing transitions at higher energies, because additional optical transitions occur at higher energies. Considering a bandgap of 465 meV, the broadened PL spectra are well reproduced for carrier densities of $0.5 \times 10^{17} \text{ cm}^{-3}$, $1.5 \times 10^{17} \text{ cm}^{-3}$ and $2 \times 10^{17} \text{ cm}^{-3}$, which correspond to pump intensities of 0.17 kW cm^{-2} , 0.35 kW cm^{-2} and 0.71 kW cm^{-2} , respectively.

Under c.w. pumping, the steady-state carrier density can be directly linked to the carrier lifetime using the generation–recombination balance law $N = I\tau/(h\nu d)$, where I is the absorbed power density, τ the non-radiative recombination lifetime, $h\nu$ the pump photon energy and d the absorption depth. To obtain the absorbed power used for calculating the carrier density and material gain, the incident power is multiplied by 0.65 to account for the disk

surface reflectivity at 1,550 nm wavelength. The extracted non-radiative lifetimes are 1.4 ns, 2.1 ns and 1.4 ns for carrier densities of $0.5 \times 10^{17} \text{ cm}^{-3}$, $1.5 \times 10^{17} \text{ cm}^{-3}$ and $2 \times 10^{17} \text{ cm}^{-3}$, respectively. The obtained values, averaged to ~ 1.6 ns, are equivalent to those reported in ref. ³. However, even with comparable lifetimes, a clearly lower pumping threshold is observed here. This remarkable feature will be discussed in the next section.

The modal gain illustrated in Fig. 3b was calculated for the carrier densities mentioned above, assuming steady-state conditions. The required parameters were obtained from the $\mathbf{k}\cdot\mathbf{p}$ band structure description, and are summarized in the Methods. At a carrier density of $0.5 \times 10^{17} \text{ cm}^{-3}$ the positive gain regime is not reached, but the gain steeply increases with the carrier density. The modal gain maximum is observed at the lasing mode energy of 485 meV. Furthermore, gain broadening is observed for larger pumping intensity due to band-filling effects. Note that the calculated modal gain might be overestimated, because it depends on unknown parameters such as homogeneous broadening. Nonetheless, these calculations indicate that modal gain can reach up to 400 cm^{-1} for carrier densities of $2 \times 10^{17} \text{ cm}^{-3}$.

Narrow WGMs appear in addition to the broad spectrum of spontaneous emission, clearly visible in Fig. 3a. The modes at 472 meV, 485 meV and 497 meV are regularly spaced by 12–13 meV and can be assigned to fundamental $\text{TM}_{19,1}$, $\text{TM}_{20,1}$ and $\text{TM}_{21,1}$ modes, respectively. Other mode patterns in the spectrum can be attributed to higher radial index modes, with $n = 2$ and $n = 3$. The $\text{TM}_{19,1}$ mode is close to the bandgap, just a few meV apart. According to gain modelling, it does not match the gain maximum. The $\text{TM}_{20,1}$ mode, at higher energy, here shows a better match. Thus, the $\text{TM}_{20,1}$ mode will dominate the spectrum at high powers. This mode competition behaviour leads to a clear single-mode laser emission.

Pulsed device results. Given that all the GeSn lasers reported in the literature were only operational under pulsed laser excitation, we also studied the properties of the present tensile-strained GeSn microdisks. This enables a comparison of GeSn lasers with moderate Sn contents and tensile strain to those reported previously in the literature with high Sn contents and residual compressive strain. Laser emission spectra taken at temperatures in the range of 25–120 K are shown in Fig. 4a. A 3.5 ns-long pulsed excitation at a fixed peak pump power of 11 mW (1 mW average pump power) was applied. Distinct differences from the c.w. excitation regime are observed. The laser spectra are multimode, with a dominant mode at 497 meV corresponding to a $2.49 \mu\text{m}$ emission wavelength. Mode assignment can be made by referencing to the spectra shown in Fig. 3a. The lasing mode at the lowest energy corresponds to the one under c.w. operation at 485 meV. The dominant mode at 497 meV is also observed at the same energy in Fig. 3a. From modelling of the WGMs, we can assign this mode to the transverse magnetic $\text{TM}_{21,1}$ mode, as the free spectral range matches the expectation from modelling. The other two modes, at 488 meV and 502 meV, are assigned to modes with a higher-order radial index, that is, $\text{TM}_{17,2}$ and $\text{TM}_{18,2}$. The modes with radial number $n = 1$ are essentially unshifted compared to those observed in the c.w. regime in Fig. 3a. Under pulsed excitation, there is a non-uniform spatial distribution of carriers and possibly also a non-equilibrium distribution over the conduction band valleys, as well as a different temperature gradient compared to c.w. excitation. The non-uniform/non-equilibrium distribution explains the shift of gain to modes with higher radial order indices. In the pulsed regime, the gain profile may indeed be different from that in c.w., enabling multimode lasing and favouring higher-energy modes. At higher temperatures, the laser spectra become single-mode (Fig. 4a), indicating a narrower frequency range of positive gain. However, more importantly, the maximum laser operation temperature in pulsed operation is almost two times higher than in the c.w. regime for the $9 \mu\text{m}$ -diameter disk.

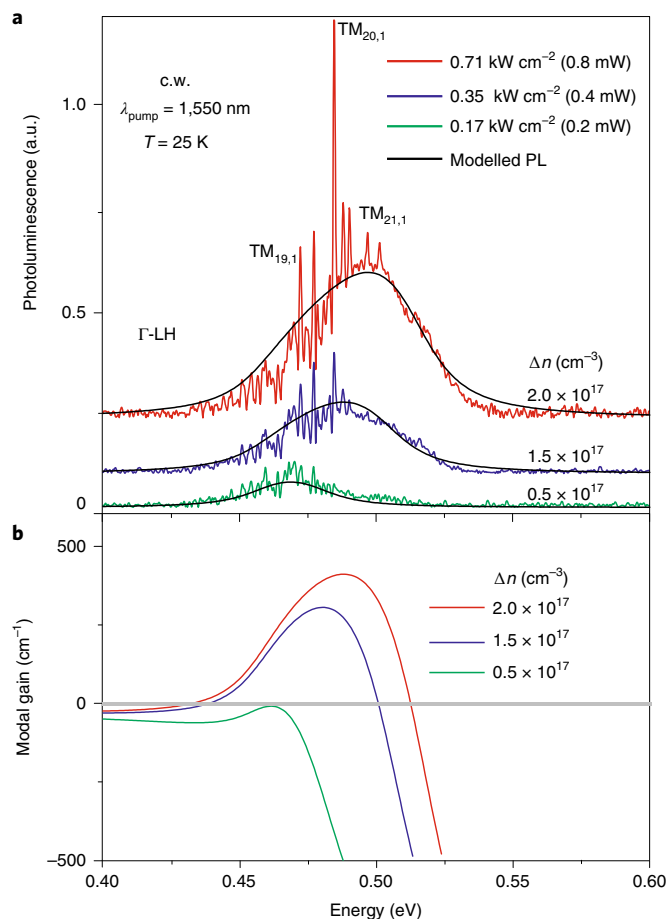


Fig. 3 | Carrier density at threshold and net gain. a, PL spectra below threshold, taken at 25 K under c.w. pumping of 0.2 mW, 0.4 mW and 0.8 mW. WGMs form on top of the spontaneous emission-dominated spectrum. The solid black lines are the calculated spontaneous emission spectra for different carrier densities. **b**, Calculated modal gain for the carrier density values from **a**.

The L–L characteristics for different temperatures are provided in Fig. 4b. Here, a thermal rollover occurs at 85 K for 20 mW peak pumping power (1.8 mW average power), compared to 5 mW at 25 K under c.w. excitation. For pulsed operation at 25 K, a lasing threshold peak power of 0.9 mW is measured (inset, Fig. 4b), which corresponds to a record low pump power density of 0.8 kW cm^{-2} . This pump power density is 250 times smaller than that of the best bulk GeSn microdisk laser reported in the literature. The threshold is temperature-dependent, as shown in Fig. 4c. A rise in temperature to 85 K increases the threshold power density to 4.2 kW cm^{-2} . At 120 K, no lasing signature is observed anymore. The maximum temperature at which the gain should still be detectable also depends on the carrier densities. Simulations of the gain for an electron/hole density of $1 \times 10^{17} \text{ cm}^{-3}$ indicate that the gain in this material becomes quite small at 120 K. Taking parasitic losses like scattering on surface roughness into account, these simulation results match the experimental observation.

In this paragraph we qualitatively discuss the laser operation mode, maximum lasing temperature and threshold pump power density for GeSn layers under tensile strain, and benchmark the results against literature data. In our experiment, where pumping is above the lasing threshold, the steady-state carrier density is expected to be nearly constant because the quasi-Fermi level is clamped by stimulated emission process. Although all electrons

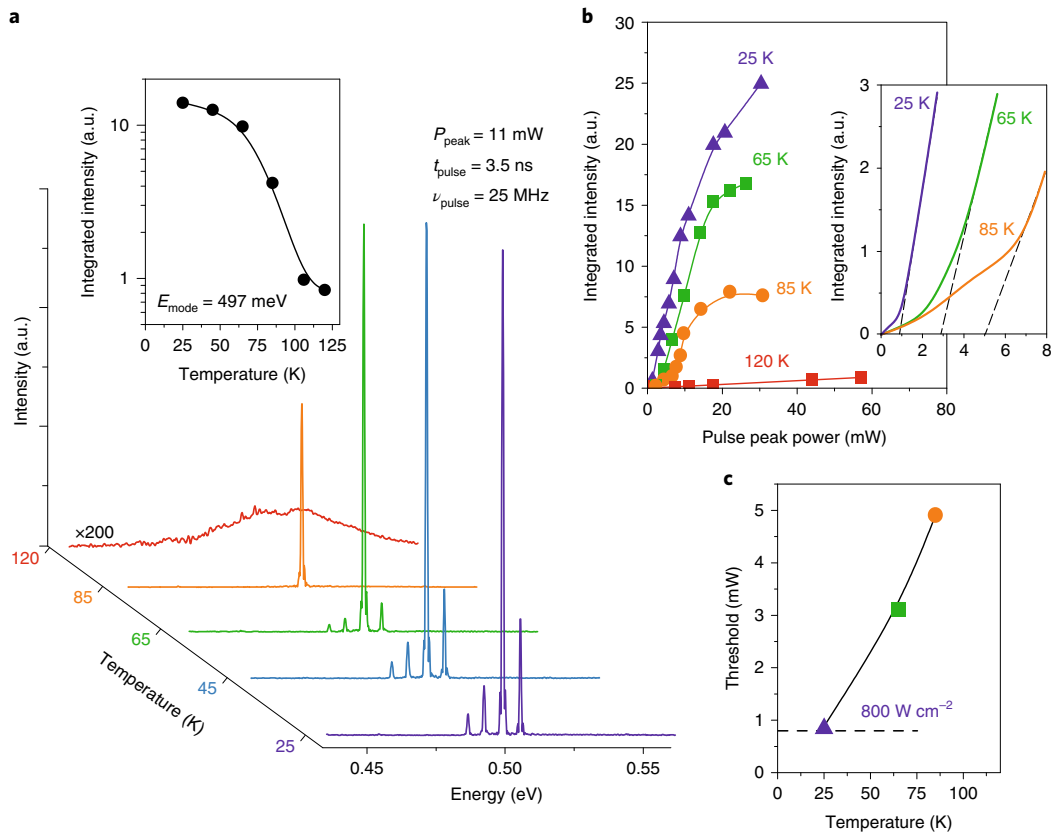


Fig. 4 | Pulsed laser. **a**, Temperature dependence of light emission of a 9-μm-diameter disk under a pulsed peak power excitation of 11 mW. Inset: integrated PL signal for the laser mode at 497 meV. **b**, L-L curves at 25 K, 65 K, 80 K and 120 K. No lasing is observed at 120 K. Inset: enlarged view of L-L curves around threshold. **c**, Lasing threshold as a function of temperature.

are generated in the Γ valley, many of them will scatter into the L valley. In particular, for a small $\Delta E_{L-\Gamma}$, here only 70 meV, and an energy difference between the quasi-Fermi level and the L valley of only 40 meV, estimated at 25 K for an electron–hole density of $2 \times 10^{17} \text{ cm}^{-3}$, a substantial amount of carriers will cool down/scatter into the L-valley. The intra- and inter-valley carrier scattering times, by phonon emission/absorption, are in the picosecond range, while the thermal relaxation time for the disk is in the microsecond range. This implies an equilibrium carrier distribution in c.w., at a lattice temperature above the nominal temperature, by ~ 20 – 30 K under 8 mW pump power (see Supplementary Information). The scattering rates increase with temperature and with the decrease of $\Delta E_{L-\Gamma}$, increasing the carrier density in the L valleys superlinearly with pump power. This leads to a decrease of the gain, because carriers in L valleys only contribute to free carrier absorption, without any contribution to gain. Moreover, as the temperature is increased, the carrier density is affected by increased non-radiative recombinations that decreases the overall gain (see Supplementary Information). Consequently, a rollover of the L–L spectrum at 25 K is observed for an excitation power exceeding 7 mW and, above 45 K, lasing is strongly quenched. These results hint to a heating of the electron bath by 40 K above the nominal sample temperature. It was experimentally observed that reducing the pump photon energy, and consequently reducing the lattice heating, leads to increased maximum operating temperatures by ~ 20 K (refs. ^{12,17}). The role of the lattice heating is underlined by the experimental observation of an increase in operation temperature by almost 30 K for the 12-μm disks. The heat dispersion by the Al pillar is then better than for 9-μm disks. Operating the same laser under pulsed excitation substantially reduces the thermal load, improving the

temperature performance of the device. Laser quenching appears above 85 K for 9-μm disks and 100 K for 12-μm disks. The increase in operation temperature for pulsed operation is only 15 K, about a half that for c.w. operation. This indicates that c.w. lasing is much more sensitive to temperature than pulsed operation. This may explain why no c.w. lasing was observed in a compressively strained GeSn laser with pumping powers 100–200 times larger than in this work. Multimode and single-mode lasing for pulsed and c.w. pumping, respectively, is probably related to an incomplete washout of spatial hole-burning by carrier diffusion, together with a larger gain, for pulsed pumping³⁷.

Next we compare the results with those for a $\text{Ge}_{0.875}\text{Sn}_{0.125}$ micro-disk laser with residual compressive strain and a similar diameter of 8 μm (ref. ⁴), emitting at almost the same energy of ~ 0.5 eV (2.5 μm) and with similar bandgap and directness $\Delta E_{L-\Gamma}$. With much stronger pump pulses, but three orders of magnitude smaller duty cycle, the average pump power and heat load were lower, so it could tolerate a larger gain drop with increasing temperature, enabling a larger maximum operating temperature of ~ 130 K. The laser active layer in this work is the thinnest reported so far, less than half that in ref. ⁴ (260 nm versus 560 nm), hence the mode overlap factors (affecting modal gain) also differ, being just 17% here and 95% in ref. ⁴. Even so, the GeSn device strained by SiN_x layers shows a substantially lower threshold.

The main achievement of the presented GeSn laser is that it enables c.w. operation. This is a direct consequence of the strongly reduced threshold power, by at least a factor of 250, which allows continuous pumping while maintaining a moderate lattice temperature. This drastic improvement is attributed to three factors: (1) the large reduction of the valence band DOS ($\Delta E_{LH-HH} = 172$ meV)

means that the population inversion is achieved at a lower density of excited carriers; (2) the modal gain of tensile-strained GeSn is improved compared to unstrained GeSn with a higher Sn content and the same $\Delta E_{L-\Gamma}$ (ref. 14); (3) the non-radiative recombination rate is substantially reduced in lower-Sn-content alloys and even more so in the present structure with the defective epitaxial interface intentionally removed during processing. Defect reduction engineering is crucial, as previously reported for GeSn/SiGeSn QW lasers¹⁷.

The above discussion should provide some guidelines for improving laser performance by combining the advantages of the present structure with those from previous GeSn laser research. An increase of the operating temperature up to 230 K was obtained by increasing the Sn content to 16 at% (ref. 7), and hence in the directness $\Delta E_{L-\Gamma}$. Tensile strain can considerably reduce the requirement for high Sn contents. A tensile strain of 1.5% in 10 at% Sn alloy results in a very large Γ population at 300 K (see Supplementary Information) and is, therefore, a viable route towards application-ready GeSn lasers. In addition, the use of SiGeSn/GeSn QW heterostructures brings additional benefits from carrier confinement and energy quantization, enabling a threshold reduction by almost an order of magnitude for strain-relaxed SiGeSn/GeSn QWs¹⁷. Heterostructures as in ref. 38, combined with tensile strain, would strongly improve the carrier confinement at higher temperatures and, consequently, further decrease the threshold pump power density. QW heterostructures yield a separation of the active region from interface defects without the use of a layer transfer technology, which is desirable for low-cost, high-yield fabrication. In the present work, bonding was used as a straightforward way to identify intrinsic material optical properties. For tensile strain engineering, however, layer transfer is also not a mandatory solution, because several previous works have shown the feasibility of using a single stressor in cavities within a fully monolithic approach^{25,26,39}. Finally, the use of stressor layers has been shown to be compatible with an electrical pumping scheme⁴⁰, which could be incorporated into the currently used layout.

Conclusion

In summary, we have demonstrated a GeSn-based laser fully embedded in a SiN_x stressor conforming layer. Starting with an indirect-bandgap GeSn alloy, by inducing tensile strain we converted it into a direct-gap optical gain material. Most importantly, c.w. and pulsed laser operation with ultra-low lasing thresholds of 0.8–1.1 kW cm⁻² have been demonstrated. These values are significantly lower than any value reported for group IV lasers and are even comparable to those for epitaxially grown III–V InP lasers⁴¹ or InGaAs lasers bonded on Si wafers⁴² (albeit the latter operate at room temperature). This achievement relies on using dilute GeSn alloys with just 5.4 at% Sn, in contrast to the mainstream research focusing on 16–20 at% Sn. Although the lower Sn content decreases the $\Delta E_{L-\Gamma}$ splitting (directness), tensile strain compensates for that and also offers a reduced DOS by shifting the LH band above the HH band. In the present work, we combine the material quality advantage of low-Sn-content alloys and the physics of tensile strain with processing technology and thermal management, enabling lasing in low-Sn-content alloys at very low pumping powers and operating in a c.w. regime. Consequently, a viable route towards room-temperature operation is predicted by combining modest Sn concentrations of ~10% with tensile strain >1% in the active layer.

Online content

Any methods, additional references, Nature Research reporting summaries, source data, extended data, supplementary information, acknowledgements, peer review information; details of author contributions and competing interests; and statements of data and code availability are available at <https://doi.org/10.1038/s41566-020-0601-5>.

Received: 28 March 2019; Accepted: 4 February 2020;

Published online: 16 March 2020

References

- Soref, R. A., Buca, D. & Yu, S.-Q. Group IV photonics—driving integrated optoelectronics. *Opt. Photon. News* **27**, 32–39 (2016).
- Thomson, D. et al. Roadmap on silicon photonics. *J. Opt.* **18**, 073003 (2016).
- Wirths, S. et al. Lasing in direct-bandgap GeSn alloy grown on Si. *Nat. Photon.* **9**, 88–92 (2015).
- Stange, D. et al. Optically pumped GeSn microdisk lasers on Si. *ACS Photon.* **3**, 1279–1285 (2016).
- Reboud, V. et al. Optically pumped GeSn micro-disks with 16% Sn lasing at 3.1 μm up to 180 K. *Appl. Phys. Lett.* **111**, 092101 (2017).
- Al-Kabi, S. et al. An optically pumped 2.5 μm GeSn laser on Si operating at 110 K. *Appl. Phys. Lett.* **109**, 171105 (2016).
- Thai, Q. M. et al. GeSn heterostructure micro-disk laser operating at 230 K. *Opt. Express* **26**, 32500–32508 (2018).
- Hodgkinson, J. & Tatam, R. P. Optical gas sensing: a review. *Meas. Sci. Technol.* **24**, 012004 (2013).
- Sieger, M. & Mizaikoff, B. Toward on-chip mid-infrared sensors. *Anal. Chem.* **88**, 5562–5573 (2016).
- Singh, V. et al. Mid-infrared materials and devices on a Si platform for optical sensing. *Sci. Technol. Adv. Mater.* **15**, 014603 (2014).
- Razeghi, M. & Nguyen, B.-M. Advances in mid-infrared detection and imaging: a key issues review. *Rep. Prog. Phys.* **77**, 82401 (2014).
- Dou, W. et al. Optically pumped lasing at 3 μm from compositionally graded GeSn with tin up to 22.3%. *Opt. Lett.* **43**, 4558–4561 (2018).
- Zhou, Y. et al. Optically pumped GeSn lasers operating at 270 K with broad waveguide structures on Si. *ACS Photon.* **6**, 1434–1441 (2019).
- Rainko, D. et al. Impact of tensile strain on low Sn content GeSn lasing. *Sci. Rep.* **9**, 259 (2019).
- Gencarelli, F. et al. Crystalline properties and strain relaxation mechanism of CVD grown GeSn. *ECS Trans.* **50**, 875–883 (2013).
- Dou, W. et al. Investigation of GeSn strain relaxation and spontaneous composition gradient for low-defect and high-Sn alloy growth. *Sci. Rep.* **8**, 5640 (2018).
- Stange, D. et al. GeSn/SiGeSn heterostructure and multi quantum well lasers. *ACS Photon.* **5**, 4628–4636 (2018).
- Du, W. et al. Study of Si-based GeSn optically pumped lasers with micro-disk and ridge waveguide structures. *Front. Phys.* **7**, 147 (2019).
- Minamisawa, R. et al. Top-down fabricated silicon nanowires under tensile elastic strain up to 4.5%. *Nat. Commun.* **3**, 1096 (2012).
- El Kurdi, M. et al. Direct band gap germanium microdisks obtained with silicon nitride stressor layers. *ACS Photon.* **3**, 443–448 (2016).
- Virgilio, M., Manganeli, C. L., Grosso, G., Pizzi, G. & Capellini, G. Radiative recombination and optical gain spectra in biaxially strained n-type germanium. *Phys. Rev. B* **87**, 235313 (2013).
- Bao, S. et al. Low-threshold optically pumped lasing in highly strained germanium nanowires. *Nat. Commun.* **8**, 1845 (2017).
- Süess, M. J. et al. Analysis of enhanced light emission from highly strained germanium microbridges. *Nat. Photon.* **7**, 466–472 (2013).
- Armand Pilon, F. T. et al. Lasing in strained germanium microbridges. *Nat. Commun.* **10**, 2724 (2019).
- Ghrib, A. et al. Control of tensile strain in germanium waveguides through silicon nitride layers. *Appl. Phys. Lett.* **100**, 201104 (2012).
- Capellini, G. et al. Strain analysis in SiN/Ge microstructures obtained via Si-complementary metal oxide semiconductor compatible approach. *J. Appl. Phys.* **113**, 013513 (2013).
- von den Driesch, N. et al. Direct bandgap group IV epitaxy on Si for laser applications. *Chem. Mater.* **27**, 4693–4702 (2015).
- Ghrib, A. et al. All-around SiN stressor for high and homogeneous tensile strain in germanium microdisk cavities. *Adv. Opt. Mater.* **3**, 353–358 (2015).
- Zaumseil, P. et al. The thermal stability of epitaxial gesn layers. *Appl. Phys. Lett. Mater.* **6**, 076108 (2018).
- Elbaz, A. et al. Solving thermal issues in tensile-strained Ge microdisks. *Opt. Express* **26**, 28376–28384 (2018).
- Elbaz, A. et al. Germanium microlasers on metallic pedestals. *APL Photon.* **3**, 106102 (2018).
- Uchida, N. et al. Carrier and heat transport properties of polycrystalline GeSn films on SiO₂. *Appl. Phys. Lett.* **10**, 232105 (2015).
- Pezzoli, F., Giorgioni, A., Patchett, D. & Myronov, M. Temperature-dependent photoluminescence characteristics of GeSn epitaxial layers. *ACS Photon.* **3**, 2004–2009 (2016).
- Cheng, R. et al. Relaxed and strained patterned germanium-tin structures: a Raman scattering study. *ECS J. Solid State Sci. Technol.* **2**, P138–P145 (2013).
- Rabolt, J. F. & Bellar, R. The nature of apodization in Fourier transform spectroscopy. *Appl. Spectrosc.* **35**, 132–135 (1981).
- El Kurdi, M. et al. Tensile-strained germanium microdisks with circular Bragg reflectors. *Appl. Phys. Lett.* **108**, 091103 (2016).

37. Sargent, M. Theory of a multimode quasiequilibrium semiconductor laser. *Phys. Rev. A* **48**, 717–726 (1993).
38. Stange, D. et al. Short-wave infrared leds from GeSn/SiGeSn multiple quantum wells. *Optica* **4**, 185–188 (2017).
39. Ghrib, A. et al. Tensile-strained germanium microdisks. *Appl. Phys. Lett.* **102**, 221112 (2013).
40. Prost, M. et al. Tensile-strained germanium microdisk electroluminescence. *Opt. Express* **23**, 6722–6730 (2015).
41. Wang, Z. et al. Novel light source integration approaches for silicon photonics. *Laser Photon. Rev.* **11**, 1700063 (2017).
42. Seifried, M. et al. Monolithically integrated CMOS-compatible III–V on silicon lasers. *IEEE J. Select. Top. Quant. Electron.* **24**, 1–9 (2018).

Publisher's note Springer Nature remains neutral with regard to jurisdictional claims in published maps and institutional affiliations.

© The Author(s), under exclusive licence to Springer Nature Limited 2020

Methods

Optical PL excitation was provided by a Nd:YAG laser at 1,064 nm wavelength focused on the sample surface with a $\times 40$ microscope objective (numerical aperture (NA) of 0.65) into a $5\ \mu\text{m}$ -diameter spot. Collection of emitted light was performed with the same microscope objective, and a beamsplitter was used to separate emission and excitation beam paths. In these experiments, we used an extended InGaAs detector to detect the luminescence. The high sensitivity, enabling the detection of low levels of infrared signals, was counterbalanced by the $2.5\ \mu\text{m}$ wavelength cutoff due to the detector response and objective transmission quenching. Lasing experiments were performed using a $\mu\text{-PL}$ set-up, with the c.w. pump laser beam at $1,550\ \text{nm}$ wavelength focused on the sample surface into a $12\ \mu\text{m}$ -diameter spot by a $\times 40$ reflective objective with NA of 0.5 and working distance of 4 mm. The same objective was used for pumping and for collection of light emitted from the microdisk. A CaF_2 beamsplitter was used to separate the excitation and emission beam paths. The outgoing emission, collected from the objective, was coupled to a Fourier transform infrared (FTIR) spectrometer equipped with a CaF_2 beamsplitter. The emission was detected by a nitrogen-cooled InSb photodetector with a cutoff wavelength $4.8\ \mu\text{m}$. The telecom wavelength pump laser was coupled out from a single-mode fibre to free space using a hyperbolic mirror, the output fibre being clamped at the focal point of the mirror. The pump can be taken through a Mach-Zehnder modulator, controlled by a radiofrequency pulse generator so that the pump beam power can be switched from c.w. to quasi-continuous and pulsed modes. The same output from a single-mode fibre was used in both cases, c.w. or pulsed, so that switching from one pump mode to another did not induce any change of the beam waist or its alignment to the disk. The pulse shape under modulated excitation had $3.5\ \text{ns}$ width and a repetition rate of $25\ \text{MHz}$. As discussed below, the pulse duration was longer than the non-radiative lifetime, so the optical excitation can be considered quasi-c.w. in this respect. The FTIR spectrometer resolution was set to $0.25\ \text{cm}^{-1}$ for linewidth narrowing analysis of the lasing mode around threshold; otherwise, it was set to $4\ \text{cm}^{-1}$.

Calculation of WGMs was performed by a two-dimensional (2D) analytical model. The resonance wavelength of the cavity mode with azimuthal index m is calculated from the roots of the m th Bessel function $J_m(\frac{2\pi n_{\text{eff}}(\lambda)}{\lambda_{\text{res}}} a)$. The optical field is plotted at the resonant wavelength to obtain the corresponding radial number of nodes, n , along the disk radius. To account for the modal dispersion of vertically confined modes, the effective index is introduced in the model, according to $n_{\text{eff}}(\lambda) = -0.6\lambda + 3.85$, where λ is the wavelength in micrometres. This expression was interpolated from 1D slab modelling of TM polarized waves propagating in the GeSn layer. The energy of the $\text{TM}_{20,1}$ mode is calculated to be $484.65\ \text{meV}$, in good agreement with the $485\ \text{meV}$ experimental value. Optical gain is calculated within the framework of the parabolic band effective mass model, using the equation²⁸

$$g(\hbar\omega) = \left| D_{\Gamma,\text{LH}}^{\text{TM}} \right|^2 \int_0^\infty \rho_{\text{LH}}(E) (f_{\text{c}}(E) - f_{\text{v}}(E)) \frac{\frac{\Gamma_0}{2\pi}}{\left(\frac{\Gamma_0}{2}\right)^2 + (E_{\Gamma,\text{LH}} + E - \hbar\omega)^2} dE,$$

where $\rho_{\text{LH}}(E)$ is the joint DOS involving the Γ conduction band and the LH valence band, and $\left| D_{\Gamma,\text{LH}}^{\text{TM}} \right|^2$ is the interband dipole matrix element. Γ_0 is the full-width at half-maximum (FWHM) of a Lorentzian function, which here is set to $25\ \text{meV}$ to account for homogeneous broadening of interband transitions, while $f_{\text{c}}(E)$ and $f_{\text{v}}(E)$ are the Fermi-Dirac functions for electrons and holes. The DOS effective masses used in the calculation were $m_{\Gamma} = 0.036 m_0$, $m_{\text{L}} = 0.56 m_0$ and $m_{\text{LH}} = 0.05 m_0$, extracted from the $\mathbf{k}\cdot\mathbf{p}$ model¹⁴ of strained GeSn with $5.4\ \text{at}\%$ Sn

content and biaxial tensile strain of 1.4% . The energy splitting $\Delta E_{\text{L}-\Gamma} = E_{\text{L}} - E_{\Gamma}$, $\Delta E_{\text{LH}-\text{HH}} = E_{\text{LH}} - E_{\text{HH}}$ and the bandgap $E_{\Gamma} - E_{\text{LH}}$ are $70\ \text{meV}$, $170\ \text{meV}$ and $465\ \text{meV}$, respectively, according to $\mathbf{k}\cdot\mathbf{p}$ modelling and PL results. Note that the DOS effective masses differ only slightly from those in pure Ge and we have therefore used the free carrier absorption model for pure Ge, assuming it would be very close to that for low-Sn-content GeSn alloy, in order to deduct it from the interband gain and find the net gain.

Reporting Summary. Further information on research design is available in the Nature Research Reporting Summary linked to this article.

Data availability

The data that support the plots within this paper and other findings of this study are available from the corresponding authors upon reasonable request.

Code availability

Finite-element modelling was performed using commercially available COMSOL software. All other calculation codes were used in published works where model details are provided. The codes are not publicly available; any requests should be sent to the corresponding authors.

Acknowledgements

M.E.K. and A.E. thank R. Colombelli and A. Bousseksou for discussions and their help with mounting the PL set-up with the FTIR spectrometer. We thank G. Mussler for XRD measurements. This work used knowledge acquired in the collaboration with H. Sigg from PSI. This work was supported by the French RENATECH network, the French National Research Agency (Agence Nationale de la Recherche, ANR) through funding of the ELEGANTE project (ANR-17-CE24-0015) and the Deutsche Forschungsgemeinschaft (DFG) via the project 'SiGeSn Laser for Silicon Photonics'. A.E. was supported by ANRT through a CIFRE grant. A.F. acknowledges funding within the ANR-16-CE09-0029-03 TIPTOP project.

Author contributions

All authors contributed to the work. P.B., M.E.K. and A.E. designed the device structure. M.E.K. and A.E. performed the strained disks fabrication with E.H., I.S., K.P. and G.P. M.E.K. and A.E. performed the PL measurements and laser experiments with N.Z. and X.C. K.P., G.P., I.S., N.v.d.D. and D.B. performed the structural analysis of the material. The GeSn layer was grown by D.B. and N.v.d.D. on substrates from J.-M.H. The Raman analyses were performed by A.F. and R.O. P.B., S.S. and Z.I. contributed to the modelling with M.E.K. and D.B. The work was supervised by D.G., F.B., P.B., D.B. and M.E.K. P.B., M.E.K., N.v.d.D., D.G. and D.B. wrote the manuscript.

Competing interests

The authors declare no competing interests.

Additional information

Supplementary information is available for this paper at <https://doi.org/10.1038/s41566-020-0601-5>.

Correspondence and requests for materials should be addressed to D.B. or M.E.

Reprints and permissions information is available at www.nature.com/reprints.

Lasing Reporting Summary

Nature Research wishes to improve the reproducibility of the work that we publish. This form is intended for publication with all accepted papers reporting claims of lasing and provides structure for consistency and transparency in reporting. Some list items might not apply to an individual manuscript, but all fields must be completed for clarity.

For further information on Nature Research policies, including our [data availability policy](#), see [Authors & Referees](#).

► Experimental design

Please check: are the following details reported in the manuscript?

1. Threshold

Plots of device output power versus pump power over a wide range of values indicating a clear threshold

Yes
 No

see CW device results and Pulsed device subsections

2. Linewidth narrowing

Plots of spectral power density for the emission at pump powers below, around, and above the lasing threshold, indicating a clear linewidth narrowing at threshold

Yes
 No

see CW device results section

Resolution of the spectrometer used to make spectral measurements

Yes
 No

See Method section

3. Coherent emission

Measurements of the coherence and/or polarization of the emission

Yes
 No

The experimental configuration did not allow measurement of the coherence but we emphasize that mode narrowing, as reported, is inherently associated to transition from incoherent to coherent emission.

4. Beam spatial profile

Image and/or measurement of the spatial shape and profile of the emission, showing a well-defined beam above threshold

Yes
 No

The disk cavity design is specific, in which WGM occurs with complex in-plane radiation pattern, beam spatial profile is not relevant in our case.

5. Operating conditions

Description of the laser and pumping conditions
Continuous-wave, pulsed, temperature of operation

Yes
 No

CW device and Pulsed device results section and Method section

Threshold values provided as density values (e.g. $W\text{ cm}^{-2}$ or $J\text{ cm}^{-2}$) taking into account the area of the device

Yes
 No

see Results section

6. Alternative explanations

Reasoning as to why alternative explanations have been ruled out as responsible for the emission characteristics
e.g. amplified spontaneous, directional scattering; modification of fluorescence spectrum by the cavity

Yes
 No

The laser threshold is clearly shown and free from doubt. The mode intensity clearly dominates the spontaneous emission background above threshold. Mode narrowing is also a clear proof.

7. Theoretical analysis

Theoretical analysis that ensures that the experimental values measured are realistic and reasonable
e.g. laser threshold, linewidth, cavity gain-loss, efficiency

Yes
 No

See discussion in the CW device results section and in the supplementary informations.

8. Statistics

Number of devices fabricated and tested

Yes
 No

We looked at 2 different disk diameters reported in the paper. A large number of devices with the same diameter or even smaller diameters were analyzed and we found very reproducible results.

Statistical analysis of the device performance and lifetime (time to failure)

- Yes
- No

We measured the same devices several times, sometimes with several days or weeks of intervals, without any changes of their characteristics. The fact that all lasers were really stable and reproducible in the investigated excitation power range, was not mentioned in the manuscript. This feature strengthens the confidence in our interpretations.